Biomedical Signal Processing and Control 79 (2023) 104247

Contents lists available at ScienceDirect

Biomedical Signal Processing and Control

journal homepage: www.elsevier.com/locate/bspc

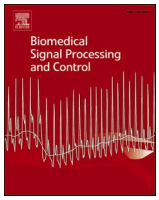

NABNet: A Nested Attention-guided BiConvLSTM network for a robust prediction of Blood Pressure components from reconstructed Arterial Blood Pressure waveforms using PPG and ECG signals

Sakib Mahmud [a], Nabil Ibtehaz [b], Amith Khandakar [a], M. Sohel Rahman [c], Antonio JR. Gonzales [a], Tawsifur Rahman [a], Md Shafayet Hossain [d], Md. Sakib Abrar Hossain [a], Md. Ahasan Atick Faisal [a], Farhan Fuad Abir [e], Farayi Musharavati [f], Muhammad E. H. Chowdhury [a,*]

[a] Department of Electrical Engineering, Qatar University, Doha 2713, Qatar
[b] Department of Computer Science, Purdue University, West Lafayette, IN 47907, United States
[c] Department of CSE, BUET, ECE Building, West Palashi, Dhaka 1205, Bangladesh
[d] Department of Electrical, Electronics and Systems Engineering, Universiti Kebangsaan Malaysia, Bangi, Selangor 43600, Malaysia
[e] Department of Electrical and Electronics Engineering, University of Dhaka, Dhaka 1000, Bangladesh
[f] Mechanical and Industrial Engineering, Qatar University, Doha 2713, Qatar

ARTICLE INFO

Keywords:
NABNet
Arterial Blood Pressure (ABP)
Photoplethysmogram (PPG)
Electrocardiogram (ECG)
BP Prediction
ABP Estimation
Signal to Signal Synthesis
Signal Reconstruction
Guided Attention
Bidirectional Convolutional LSTM
1D-Segmentation

ABSTRACT

Background: **and Motivations:** Continuous Blood Pressure (BP) monitoring is crucial for real-time health tracking, especially for people with hypertension and cardiovascular diseases (CVDs). The current cuff-based BP monitoring methods are non-invasive but discontinuous while continuous BP monitoring methods are mostly invasive and can only be applied in a clinical setup to patients being monitored by advanced equipment and medical experts. Several studies have reported different techniques for predicting BP values from non-invasive Photoplethysmogram (PPG) and Electrocardiogram (ECG) signals. Apart from BP readings, estimating ABP waveforms from non-invasive signals can provide vital body parameters such as Mean Arterial Pressure (MAP) which can be used to determine poor organ perfusion, nutrient supply to organs, and cardiovascular diseases (CVDs), etc.

Methods: It is challenging to estimate ABP waveforms while maintaining a high BP prediction performance and ABP waveform pattern. In this work, we propose a novel approach for ABP waveform estimation by separating the task into BP prediction and a normalized ABP waveform estimation through segmentation from PPG, PPG derivatives, and ECG signals, and combining afterward. We propose the Nested Attention-guided BiConvLSTM Network or NABNet which uses LSTM blocks during segmentation for better handling of the existing phase shifts between PPG, ECG, and ABP signals. Several experiments were performed to improve the ABP reconstruction performance, which was combined with an existing BP prediction pipeline for the non-invasive estimation of ABP waveforms.

Results: The proposed framework can robustly estimate ABP waveforms from PPG and ECG signals by reaching a high MAP performance and low construction error while maintaining the overall Grade A performance of the BP prediction pipeline.

Conclusion: Linearly translating the range-normalized, synthesized ABP segments by corresponding SBP and DBP predictions from the BP prediction pipeline managed to robustly estimate ABP waveforms from PPG and ECG signals.

* Corresponding author.
E-mail address: mchowdhury@qu.edu.qa (M. E. H. Chowdhury).

https://doi.org/10.1016/j.bspc.2022.104247
Received 22 February 2022; Received in revised form 25 August 2022; Accepted 18 September 2022
Available online 24 September 2022

1. Introduction

Cardiovascular Diseases (CVDs) are the leading cause of death around the world according to World Health Organization (WHO) [1]. Around 17.9 million lives are being lost worldwide due to CVDs every year, which is approximately 32% of the total death Worldwide [2]. CVD can be of many types such as coronary heart disease, cerebrovascular disease, rheumatic heart disease, etc. More than 85% of CVD-related deaths cause heart attacks and strokes [3] and high Blood Pressure (BP) or hypertension [4]. Long-term continuous BP monitoring can dynamically reflect the change in one's health condition, thus predicting and helping in preventing potential complexities [5,6]. Recently, BP and heart rate monitoring systems showed great promise in diagnosing and monitoring CVDs [7,8]. Commonly used clinical BP measurement techniques involve auscultation and cuff-based oscillometric techniques, which are non-invasive but discontinuous. Traditional ambulatory practices use the oscillometric method for BP measurement, which involved repeated inflation of the cuff around the arm. Such procedures cause discomfort, disturbance during rest, and even pain for some patients. They also cannot be applied to patients with existing complexities such as "Lymphedema" [9]. Thus, the demand for a robust, cuffless method for measuring BP has significantly increased even in a clinical setup. Despite the need, no commercially available device has been approved in clinics for continuous and non-invasive BP measurement. Currently, the gold standard for real-time, continuous, and accurate BP monitoring is done by inserting a small catheter called an "Arterial Line" into a patient's artery [10], which captures Arterial Blood Pressure (ABP) waveform and BP metrics are extracted from the ABP signal. This approach is not suitable for wearable systems or in-home settings due to the invasiveness, complexity, advanced equipment, and medical expertise requirement in the process. On the other hand, certain high-risk CVD conditions such as "masked", or "white-coat" hypertension cannot be identified just from auscultatory or oscillometric techniques using only BP metrics rather it requires continuous monitoring of the ABP waveforms [11]. Additionally, Mean Arterial Pressure (MAP) recorded from ABP waveforms can be used to identify poor organ perfusion. MAP can be used to determine overall blood flow and the level of nutrient delivery to an organ, thus often used in critical conditions such as "Septic Shock [12]. Too low MAP can lead to shock, syncope, or poor organ perfusion. On the contrary, too high MAP exerts stress on the cardiovascular system and might even lead to CVDs [13]. For these reasons, it is important to develop improved methods for continuous and non-invasive ABP monitoring (additional to BP monitoring), especially for high-risk patients in both clinical and home settings.

In recent years, Machine Learning (ML) based techniques have been used extensively to predict BP from Photoplethysmogram (PPG) and/or Electrocardiogram (ECG) signals [14–20]. The initial approach for predicting BP largely comprised of manually extracting features such as physiological parameters and PPG signal features [17], amplitude and phase information of PPG signals [18], Womersley Number [14,15], Level-Crossing Features (LCFs) from the derivatives of PPG signals [19] and then, apply ML-based regression algorithms on the extracted features for the BP prediction. Popular Pulse Transit Time (PTT) based methods [14,21,22] are effective for healthy individuals and outpatients but not so much for inpatients, especially patients in the Intensive Care Unit (ICU). These methods largely suffer from various time-domain feature-related issues since their accuracy gets affected by several factors and requires frequent recalibration [23]. Due to the ability of the ML algorithms to learn intricate features from the signals in a dataset, they solved the drawbacks of traditional PTT-based approaches. ML algorithms such as Multilayer Perceptron (MLP) [18,24,25], and other traditional algorithms, such as Support Vector Machine (SVM) [15,26], Random Forest (RF) [15,16,17,27], Decision Trees [28], Adaptive Boosting (AdaBoost) [17], Gradient Boosting (GradBoost) [29], etc. have been used extensively in this domain. More recent studies tried to use Deep Convolutional Neural Networks or Deep CNNs for BP prediction [30–45]. Since Deep CNNs can extract latent features automatically, challenges and limitations faced in manual extraction of features were avoided. For this reason, even though some of the Deep Learning-based approaches worked on features [27,42] most of them worked on raw signals. Esmaelpoor et al. [43] proposed an interesting pipeline where they extracted features using a CNN model and applied LSTM on the features to extract BP information, which greatly inspired our previous work [44].

Now, continuously predicting true MAP (true MAP is not estimated from discrete SBP and DBP values, rather it is the mean of the ABP waveform itself) requires ABP signals to be present in the dataset. ABP being an invasive signal is not easy to collect in a normal setup unlike PPG and ECG and requires clinical intervention and Institutional Review Board (IRB) approval for data acquisition. The Medical Information Mart for Intensive Care III (MIMIC-III) dataset [46] provides clinical and waveform data from several thousand patients containing data for several vital body parameters and some physiological signals, such as PPG, ECG, and ABP. Based on the MIMIC-III dataset and some private datasets, several studies tried to predict MAP, SBP, and DBP [27]. Until very recently, a few studies aimed at estimating the ABP waveform itself [31,32,36,37–39,41,45]. Robustly estimated ABP waveforms could provide all vital BP information along with waveform patterns containing valuable cardiovascular information. Literature shows that both PPG [47] and ECG [48] can be used for the early detection of CVDs such as Atrial Fibrillation. Now, PPG and ABP are intrinsically related [49,50], which is the primary idea behind using PPG features to predict BP values and estimate ABP waveforms. On the other hand, adding ECG with PPG provides the system with features such as Pulse Arrival Time (PAT) and Pulse Transit Time (PTT) which deep convolutional neural networks can learn during training. Thus, estimated ABP signals from PPG and ECG have the potential to inform early about cardiovascular anomalies alongside BP parameters, provided that the estimation is correct. This makes it more important to design a system that can robustly estimate ABP waveforms in all types of situations.

With the advancement of technology, PPG and ECG can be acquired non-invasively and in recent times, there have been smart wearable technologies that can make the process much more comfortable and accessible [51]. Implementing a robust model with such a system will provide ABP waveforms in real-time. Most recent studies proposed several Deep ConvNets and ML pipelines for estimating ABP from PPG and/or ECG. But the challenge often faced by the researchers was the absolute magnitude of the ABP waveforms. It is not straightforward to estimate ABP directly using deep networks since they are the most efficient in the normalized form [52–53]. While PPG and ECG can be normalized and still retain almost all vital features (performed in most studies in the literature), ABP waveforms contain BP information for which a normalized ABP waveform does not have many usages except probably anomaly detection from the pattern. Ibtehaz et al. [32] and Athaya et al. [31] in their studies tried to estimate ABP from PPG using U-Net based 1D-Segmentation model. Both studies normalized the ABP signals using the min–max technique using global maximum and minimum during training and denormalized after prediction through a linear transformation. This procedure is challenging since we do not know the denormalization factor. Even though it made the process standard, due to transforming all the signals with the same factor, it produced high errors, especially for signals with BP values far from the global factors. On other hand, the existing phase-shift or time delay between PPG, ABP, and ECG signals might also affect the segmentation performance. 1D-segmentation networks provide the best signal synthesis performance when the model can easily map the features of the target signals to the predictor signals one-to-one. Harfiya et al. [37] tried to directly estimate ABP from PPG using a Long Short-Term Memory (LSTM) based neural network, where they discussed in detail the effect of phase-shift between PPG and ABP signals during segmentation and how they dealt with it. Qin et al. [36] proposed Deep Variational Autoencoder with Domain

Adversarial Training (RDAE) model for PPG to ABP estimation where ABP signals were normalized and reversed using global z-score parameters (mean, standard deviation). In a very recent study, Mehrabadi et al. [45] used Cycle Generative Adversarial Network (CycleGAN) to estimate ABP from PPG where the normalization procedure was not explained in detail.

Therefore, in this study, we propose a method where we synthesize normalized ABP waveform patterns from non-invasive PPG and ECG signals and linearly transform them to ABP waveforms using BP values predicted using a BP prediction model. We also propose a novel segmentation architecture called NABNet which efficiently uses CNN-based Bi-Convolutional LSTMs and Guided Attention to mitigate the phase-shift issue between PPG and ABP and improve segmentation performance. The main contributions of this study are summarized as follows:

- To overcome the challenges in ABP estimation, we propose a hybrid pipeline that separates the ABP estimation process into two parts viz. BP prediction and ABP pattern estimation. The estimated normalized ABP patterns are linearly transformed into ABP signals using their respective BP metrics.
- We propose the NABNet architecture which utilizes Convolutional LSTM and Attention Guidance concepts for improving construction error accumulating due to ABP phase lag during segmentation.
- This study performs multiple sets of experiments to determine the best segmentation model for ABP estimation. The model is trained on a large, variable dataset with highly varying PPG and ECG waveforms to enhance the robustness and generalizability of the model.

The rest of this study is organized as follows: after an introduction and brief literature review in section I, materials and methods are explained in section II. Section III describes the experiments performed to explore the best ABP estimation model. Section IV discusses the experimental results and Section V concludes the article.

2. Methodology

In this section, we briefly explain the methodology followed in this study in detail. At first, we discuss the proposed ABP signal estimation framework and the rationality behind it. Then we elaborate on the architecture of our proposed NABNet for deep learning-based segmentation.

2.1. Proposed approach for ABP signal estimation

The proposed pipeline shown in Fig. 1 is a combination of the BP prediction pipeline proposed in [44] and the ABP signal pattern estimation pipeline explored in this study. Since ABP waveforms have much higher amplitudes compared to PPG and ECG waveforms and their absolute amplitudes carry vital information such as SBP, DBP, or MAP, it is inadequate if only the patterns are estimated. But the deep segmentation pipelines cannot properly handle such discrepancies in terms of amplitude between the target and the estimators. So, we divided the overall procedure into two sections which are combined later. The purpose of the BP prediction pipeline is to just estimate SBP and DBP values i.e., the signal amplitudes while the ABP segmentation pipeline tries to estimate the ABP patterns from PPG and ECG.

BP Prediction: The BP prediction sub-pipeline can utilize any efficient BP prediction method. The accuracy of the final estimated ABP signals will largely depend on the predicted BP values in this stage since segmented normalized ABP patterns are linearly transformed using corresponding BP values. In this study, we used the BP predictions from the shallow U-Net-based autoencoder proposed in [44].

ABP Waveform Pattern Estimation: The PPG, ECG, and ABP signals used to train the segmentation model were range normalized between 0 and 1. The aim was to use a 1D segmentation network to estimate the ABP waveform patterns by leveraging PPG and ECG features while boosting the performance by working on target signals normalized in the same range as the predictor signals. Since this pipeline is an ensemble of two sub-pipelines (Fig. 1), the error can be generated from any one of them. For instance, if the BP prediction is highly erroneous, the estimated ABP will also have higher errors. On the other hand, if the estimated ABP patterns are not matching to their ground truths by a large margin or there is a high phase shift, the final estimated ABP waveforms will have a high error in Mean Arterial Pressure (MAP) prediction since that value depends on the pattern and absolute position of the signals. But the error contributions are different for each pipeline, and it affects observing parameters (SBP, DBP, and MAP) differently. The pipeline needs to be robust enough to minimize error contribution from both sub-pipelines. Even though all the predictor signals during ABP pattern estimation were range normalized, the synthesized ABP patterns from the segmentation network might not be exactly between 0 and 1, which would cause error propagation. To ensure that all estimated ABP signals are between 0 and 1, they need to be range normalized again before linear transformation which retains the BP prediction performance even in the ABP signals. In other words, if all estimated ABP signals are not ranged exactly between 0 and 1, linearly

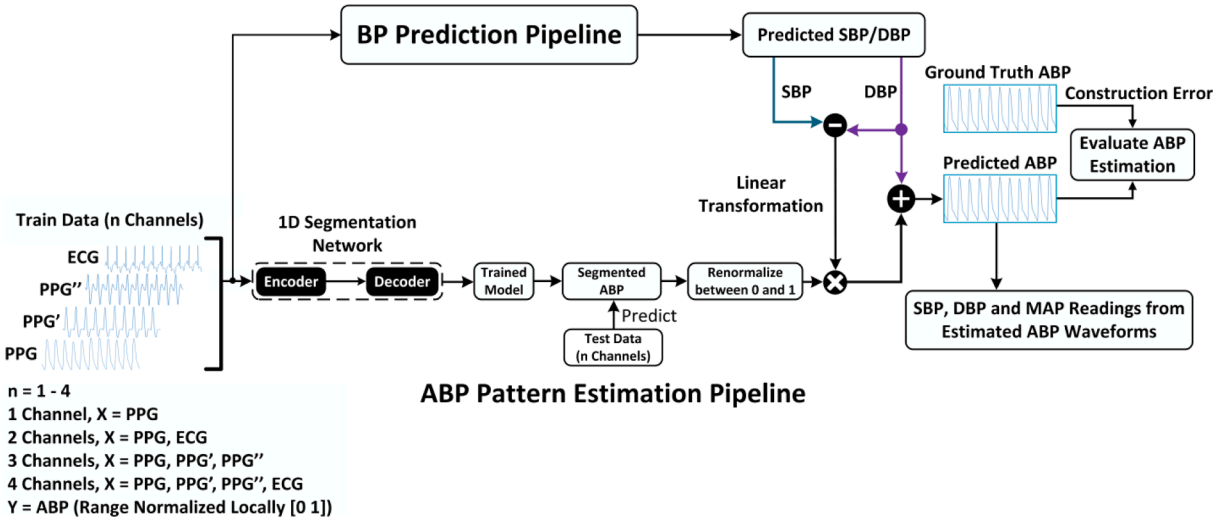

Fig. 1. Flowchart showing the end-to-end pipeline for ABP signal estimation.

transforming them will destroy the BP prediction performance achieved earlier. Finally, the reconstructed normalized ABP patterns are denormalized through a linear transformation using corresponding BP values from the BP Prediction pipeline following **Equation (1)**.

$$\boldsymbol{ABP}_i = \{\boldsymbol{ABP}_{i(norm)} * (SBP_i - DBP_i)\} + DBP_i \tag{1}$$

Here, 'i' denotes the corresponding i_{th} outcome from both sub-pipelines. Vectors are differentiated from the scalars by bolding. The normalized ABP patterns are multiplied by the difference between SBP and DBP before being added by DBP to get the estimated ABP waveforms.

2.2. Overview of proposed NABNet

In this paper, we propose Nested Attention Guided Bi-Convolutional LSTM Net (NABNet in short), a 1D-CNN-based Segmentation Architecture that utilizes Attention Guided LSTM (AG-LSTM) block to properly segment slightly phase-shifted signals such as PPG and ABP. NABNet architecture (Fig. 2) is built on the UNet++ framework proposed in [54]. But in place of direct skip connections, Attention Guided Bi-Convolutional LSTM (BiConvLSTM) blocks (Fig. 3**(a)**) were used to reduce the semantic gaps not only among the encoders (green circle) and the decoders (purple circle) but also in the middle blocks (orange circle). The NABNet architecture uses a modified version of the Additive Attention Gate (AG) module proposed in [55] for image segmentation using UNet, followed sequentially by a BiConvLSTM block [56–58].

NABNet Modified Attention Guided LSTM Block: For NABNet, the Modified Guided Attention (MGA) sub-module (Fig. 3**(a)**) is placed sequentially with the BiConvLSTM block. Inside the Attention Guided LSTM block of NABNet (masked as 'Blue' in the NABNet architecture shown in Figs. 2 and 3**(a)**), at first spatial support is removed from both gating vectors $\mathbf{g^l}$ and skip connections $\mathbf{x^l}$ by passing them through '1x1x1 Convolution' blocks, thus reducing trainable parameters and computational complexity during linear transformation afterwards. The skip connections are downsampled to the resolution of the gating signal with a stride of 2 during convolution. The weights and Biases of this operation can be formulated as $W_x^T x_i^{l,down} + W_g^T g_i + b_g$, where $\mathbf{W_x^T}$ and $\mathbf{W_g^T}$ correspond to the weights of the skip connection(s) and gating signal, respectively; $\mathbf{b_g}$ is the combined bias from both terms. Following the linear transformation (here, element-wise addition), there is a non-linear activation function is placed sequentially to condition the model predictions on a large receptive field. In this case, Rectified Linear Unit (ReLU), denoted by σ_1, has been used as the non-linear function. For ReLU, $\sigma_1\left(x_{i,c}^l\right) = \max(0, x_{i,c}^l)$, where 'i' and 'c' denote spatial and channel dimensions, respectively. ReLU is followed by a '1x1x1 Convolution' block termed as ψ, with a bias term $\mathbf{b}_\psi$. The process up to this point is combined and called as $\mathbf{q_{att}^l}$ in **Equation (2)**. In the original implementation, trilinear interpolation was used as the resampler [55]. In this implementation, there are two resamplers, one uses the interpolation-based UpSampling technique, and another uses Transposed Convolution for resampling. Then they are added element-wise to produce the final Attention Coefficient, 'α'. From literature, transposed convolution, which is like a reversed version of the convolutional operation, resamples the coarser features differently than the traditional interpolation techniques [59]. Some architectures such as DenseInceptionUNet [60] achieved higher performance by resampling the coarser features from lower layers using both techniques parallelly and adding them up before concatenation during up-sampling which reduced feature loss. Here, let's, $\mathbf{h_{nxn}^2}(\bullet)$ denotes the Transposed Convolution layers with strides = 2 and $\mathbf{u^2}(\bullet)$ denotes the UpSampling block. This operation can be formulated as in **Equation (3)**. The 'Sigmoid' activation function (σ_2) is used before resampling to range normalize the Attention Coefficients between 0 and 1. Sigmoid activation function, which can be formulated as $\sigma_2(x_{i,c}) = \frac{1}{1+\exp(-x_{i,c})}$, has been used in both resampler branches (**Equation (4)**). So, the Modified Attention Guided module can be formulated with the set of equations as follows:

$$q_{att}^l = \psi^T\left(\sigma_1\left(W_x^T x_i^{l,down} + W_g^T g_i + b_g\right)\right) + b_\psi \tag{2}$$

$$y^{l+1} = h_{1x1}\left(y^l\right) \oplus u^2\left(y^l\right) \tag{3}$$

$$\alpha_i^l = h_{1x1}\left(\sigma_2\left(q_{att}^l\left(x_i^{l,down}, g_i; \Theta_{att}\right)\right)\right) \oplus u^2\left(\sigma_2\left(q_{att}^l\left(x_i^{l,down}, g_i; \Theta_{att}\right)\right)\right) \tag{4}$$

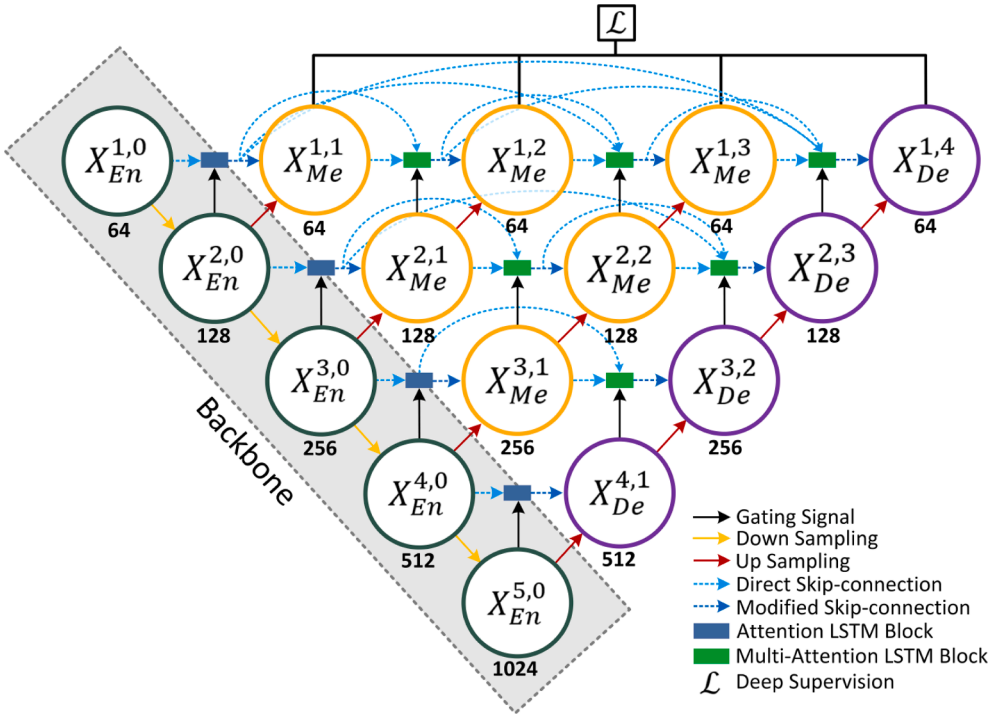

Fig. 2. Proposed NABNet Model Architecture.

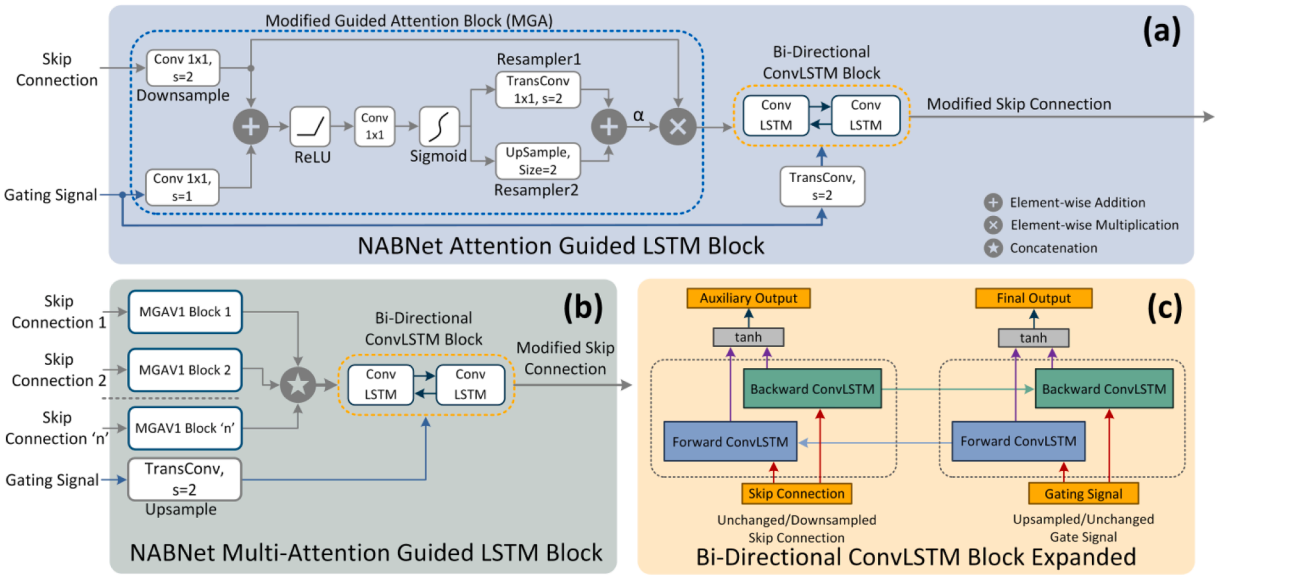

Fig. 3. (a) NABNet Attention Guided LSTM Block; **(b)** NABNet Multi-Attention Guided LSTM Block; **(c)** Bi-Directional Convolutional Long Short-Term Memory (BiConvLSTM) Block Expanded.

Here, $\oplus$ denotes element-wise addition. The MGA block outputs the element-wise multiplication ($\otimes$) of the input feature maps $\mathbf{x}^{\mathbf{l,down}}$ as shown in **Equation (5)**, and the attention coefficients, $\alpha_i \in [0,1]$, i.e.,

$$x^{l+1} = \left(x^{l,down} \otimes \alpha_i^l\right) \tag{5}$$

The BiConvLSTM block (Fig. 3**(c)**) takes in both the attention-guided feature maps $\mathbf{x}^{\mathbf{l+1}}$ from the MGA block and the upsampled (Interpolation or Transposed Convolution) gating signal $\mathbf{g}^{\mathbf{l,up}}$ to produce the final modified skip connection and forwards it to the next convolutional blocks. The BiConvLSTM block consists of two ConvLSTM blocks in contrast to traditional fully connected LSTM (FC-LSTM) blocks. ConvLSTM uses convolution for input-to-state and state-to-state conversion, thus saving more spatial information. ConvLSTM consists of an input gate ($\mathbf{i}^{\mathbf{l}}$), a forget gate ($\mathbf{f}^{\mathbf{l}}$), a memory cell ($\mathbf{c}^{\mathbf{l}}$), an output gate ($\mathbf{o}^{\mathbf{l}}$), and a hidden state ($\mathbf{H}^{\mathbf{l}}$), which can be formulated using **Equation (6)**:

$$i^l = \sigma_1\left(W_{xi} * m^l + W_{hi} * H^{l-1} + W_{ci} \circ c^{l-1} + b_i\right) \tag{6.1}$$

$$f^l = \sigma_1\left(W_{xf} * m^l + W_{hf} * H^{l-1} + W_{cf} \circ c^{l-1} + b_f\right) \tag{6.2}$$

$$c^l = f^l \circ c^{l-1} + i^l \circ \tanh\left(W_{xc} * m^l + W_{hc} * H^{l-1} + b_c\right) \tag{6.3}$$

$$o^l = \sigma_1\left(W_{xo} * m^l + W_{ho} * H^{l-1} + W_{co} \circ c^l + b_o\right) \tag{6.4}$$

$$H^l = o^l \circ \tanh\left(c^l\right) \tag{6.5}$$

Here, * and $\circ$ represents convolution and the Hadamard function, respectively. $\mathbf{m}^{\mathbf{l}}$ is the input tensor consisting of $\mathbf{g}^{\mathbf{l,up}}$ and $\mathbf{x}^{\mathbf{l+1}}$. $\mathbf{W_{xi}}$ and $\mathbf{W_{hi}}$ correspond to the 2D convolution kernel of the input state and hidden state, respectively. $\mathbf{b_i}$, $\mathbf{b_f}$, $\mathbf{b_c}$ and $\mathbf{b_o}$ are four bias terms.

NABNet Multi-Attention Guided LSTM Block: Here, for the encoder blocks, only one skip connection is forwarded to the next blocks. So, a single MGA block is adequate. But for the blocks where multiple skip connections arrive from other blocks on the same level, they need to be guided properly. One way is to concatenate all of them and perform guided attention to the concatenated signal, as proposed in [61], the other is Multi-Scale Attention Module (MSAM) [62] where each feature map is downsampled into more than two stages, then upsampled, added, convolved and concatenated gradually to get the output feature map. On the contrary, in this case, all skip connections were guided separately. In the Multi-Attention Guided LSTM Block for NABNet (Fig. 3**(b)**, masked as 'Green' in Fig. 2), outputs from several MGA blocks (one MGA block for each skip connection) are concatenated and sent to a BiConvLSTM block for the final modified skip connection and forwarded to the next blocks. If various skip connections can be denoted as '**k**', then this procedure for 1 to '**n**' skip connections can be formulated as in **Equation (7)**,

$$x^{l+1} = \prod_{k=1}^{n} \left(x_k^{l,down} \otimes \alpha_k^l\right) \tag{7}$$

Here, 'Π' denotes the concatenation operation. Then, the concatenated feature map is fed to a BiConvLSTM block along with the upsampled gating signal, similar to a single MGA block.

3. Experimentation and results

In this section, first, the dataset used in this study and data pre-processing steps will be explained before reflecting on the experimental setup developed for ABP estimation. Next, the qualitative and quantitative experimental evaluation outcomes of this study are presented. Finally, the quantitative results are compared to the current literature.

3.1. The Cuff-Less Blood Pressure estimation dataset, a subset of MIMIC-III

The primary dataset used for this study has been used in [44] and is also available in this GitHub repository [63]. This dataset [63] was extracted and pre-processed from "The Cuff-Less Blood Pressure Estimation Dataset" [64] (termed as the "UCI Dataset" in this paper) prepared by Kachuee et al. [26] and stored in the UCI Machine Learning Repository [65] containing 12,000 PPG, ECG, and ABP records divided into four parts (3000 records in each). The data pre-processing steps have been discussed in detail in [44]. A summary of the dataset used in this study is provided in Table 1.

Table 1
Overview of the datasets (after pre-processing).

Dataset	Parameters	Minimum	Maximum	Mean	SD
UCI	SBP	76.979	189.984	132.451	21.590
	DBP	50.000	121.451	63.928	9.979
	MAP	59.938	147.000	87.620	12.815

The dataset we used in this study is a subset of the MIMIC-III Waveform Dataset [46] shared in the UCI Database [65] by Kachuee et al. [26]. Another version of this dataset has been shared in Kaggle [66] by the same authors. The dataset has 12,000 records extracted and pre-processed from the MIMIC-III dataset from several unique subjects. Even though one or multiple records from the same subject are present in the dataset, the records of the same patients in this dataset are presented sequentially. Since the dataset is not shuffled before splitting, it was ensured that the data from the same patients are not present in train and test sets. It minimizes the risk of the subject-wise data leaking problem. We also performed 4-fold cross-validation by keeping data from one entire part as the test set in each fold to minimize the risk of leaking. For this study, three parts of the UCI dataset were combined to make the train set (9000 Records, roughly 75% of the dataset). The remaining part was taken as the test set (3000 Records) making it four-fold cross-validation. During training, randomly selected 20% of the training set was used for validation. A description of the train and test sets used in this experiment is provided in Table 2.

In **Appendix A**, we also provide histograms and box plots (**Supplementary Figure S1**) showing the distribution of SBP, DBP, and MAP of each part of the UCI dataset, and the description of train and test sets of each of the four folds (**Supplementary Table S1**). From **Supplementary Table S1**, it can be seen that for all folds, SBP, DBP, and MAP parameters of the test set closely match that of the train set. The sampling rate of all the signals from the UCI dataset (i.e., MIMIC dataset) is 125 Hz and was segmented as 1024 sample points (length) per segment. So, the duration of a single segment is approximately $(1024/125) \approx 8.192$ s. The final preprocessed dataset contains around 191,198 segments, which makes the total duration of the dataset to be around $\frac{191198*8.192}{60*60} \cong$ 435 hours.

3.2. Data Pre-processing

The dataset prepared for this work followed the pre-processing steps done in this paper [44] on the UCI dataset [26]. The signals were filtered and baseline corrected, bad signals were removed based on the criteria and thresholds mentioned in [44], two derivatives of PPG were derived and aligned for each segment, and finally, all four channel signals along with their respective BP ground truth and metadata were saved. Following [44] and other similar studies [32–33,37], all records outside the DBP range of (50–120), SBP range of (75–190), and BP difference of (20–120) were discarded to get rid of extreme values. The only extra data pre-processing steps followed in this work consisted of the respective normalization techniques of the ABP signals for the 'BP prediction' and the 'ABP pattern recognition' sub-pipelines.

Normalization: PPG and ECG signals were at first 'z-score' normalized, then range normalized between 0 and 1 per segment (**Equation (8)**) for both pipelines. For the BP prediction task, ABP waveforms were min–max normalized (**Equation (9)**) after being 'z-score' normalized by dividing the samples by the maximum SBP value from the whole dataset (globally normalized), following the procedures of [44],

$$\mathbf{ABP}_i(\mathrm{norm}_{\mathrm{ABP}}) = range\left(\left(\frac{\mathbf{ABP}_i - \mu_i}{\sigma_i}\right), [0\ 1]\right) \tag{8}$$

Table 2
Description of Train and Test Sets.

No. of Channels	Predictors	Target	Number of Segments	
			Train Set	**Test Set**
1	PPG	ABP	9000 Records	3000 Records
2	PPG, ECG			
3	PPG, VPG, APG			
4	PPG, VPG, APG, ECG			

On the other hand, for the ABP signal pattern estimation pipeline, ABP signals were normalized following the same process as PPG and ECG waveforms (**Equation (8)**) since it was noticed that keeping all the signals within the same range removes any bias present in the dataset and provides with the best segmentation performance. Here, for equations and pseudo-codes, signal vectors are written in **Bold** while MATLAB built-in functions are written in *Italic*.

$$\mathbf{ABP}_i(\mathrm{norm}_{\mathrm{BP}}) = \frac{\mathbf{ABP}_i}{\mathrm{SBP}_{\text{Global Maximum}}} \tag{9}$$

For one of the ablation studies, the phase shift between PPG, ECG, and ABP signals has been minimized based on an algorithm provided as a pseudo-code in **Appendix B** along with a sample visualization before and after phase shift correction in **Supplementary Figure S2**.

3.3. Quantitative evaluation

In this section, we quantitatively evaluated the performance of NABNet in reconstructing ABP waveform patterns from PPG and ECG compared to other state-of-the-art segmentation networks. The performance of the networks in estimating ABP patterns is evaluated through the commonly used construction error metric for signal reconstruction on range normalized signals. BP prediction performance is evaluated through the standard metrics from the British Hypertension Society (BHS). Details about the BHS standard are provided in **Appendix C**. We also performed some statistical analysis on the BP prediction performance.

Construction Error and BHS Metric: Mean Absolute Error (MAE) were used as the primary evaluation metric for this study. For predicted signals $\widehat{Y} = [\widehat{Y}_1, \widehat{Y}_2, \widehat{Y}_3, \cdots, \widehat{Y}_n]$ and ground truth signals $Y = [Y_1, Y_2, Y_3, \cdots, Y_n]$, MAE is defined as in **Equation (10)**,

$$\mathrm{MAE} = \frac{\sum_{i=1}^{n} |Y_i - \widehat{Y}_i|}{n} \tag{10}$$

Here, 'n' is the total number of data points. Now, unlike BP prediction, where the predictions are single data points, here, we are predicting the whole ABP waveforms. So, error measurement was applied to the signal vectors as a whole, which is termed the "Construction Error". MAE-based Construction Error can be defined as in **Equation (11)**,

$$\text{Construction Error} = \frac{\sum_{i=1}^{n}\left(\frac{\sum_{j=1}^{m} |Y_{ij} - \widehat{Y}_{ij}|}{m}\right)}{n} \tag{11}$$

Here, 'm' is the number of samples or data points in each segment, which is 1024 for this study and 'n' is the total number of segments. So, construction error considers the whole signal while computing the metric, and it is a very important secondary evaluation metric for studies concerning signal reconstruction. We computed the construction error for both normalized and final ABP waveforms and presented it in Table 3 alongside the BP prediction performance in terms of the BHS metric. The main aim of designing the NABNet was to optimize MAP prediction performance by reducing the phase shifts among segments while lowering construction error through Nested Attention Guided BiConvLSTM blocks. Upon comparing the Performance of multiple state-of-the-art segmentation networks, NABNet was found to be the most efficient in terms of both construction errors and BHS metrics.

Apart from MAP, around 92% and 99% of the estimated ABP waveforms for all networks met the BHS Grade A requirements for predicting SBP and DBP, respectively (Detail in **Appendix C**, **Supplementary Table S2**). These performances are the same as the BP prediction performance from the shallow UNet-based autoencoder proposed in [44] since the currently proposed pipeline is designed in such a way that there is no performance loss.

Performance against the AAMI standard: According to the Association for the Advancement of Medical Instrumentation Standard

Table 3
Performance Evaluation in terms of Construction Error and BHS Metric.

1D-CNN Segmentation Networks	Construction Error (Norm ABP Signal)		Construction Error (Final ABP Signal)		BHS Metric (MAP)		
	Mean	SD	Mean	SD	Grade A	Grade B	Grade C
UNet [67]	0.077	0.043	4.930	2.570	85.01	99.72	99.97
Attention UNet [55]	0.075	0.043	4.784	2.530	86.46	99.78	99.99
Ensembled UNet [54]	0.078	0.043	5.060	2.533	85.71	99.65	99.97
UNet+ [54]	0.076	**0.042**	4.851	2.509	86.91	99.69	99.99
UNet++ [54]	0.076	0.043	4.826	2.626	85.71	99.70	99.99
MultiResUNet [68] (alpha = 1)	0.076	0.044	4.870	2.457	86.49	99.78	99.99
DenseInceptionUNet [60] (Dense Loop = 2)	0.077	0.044	4.945	2.651	86.66	99.61	99.98
BCDUNet (D = 3) [56]	0.075	0.045	4.804	2.680	86.83	99.75	99.99
SEDUNet (D = 3) [57]	0.075	0.047	4.790	2.715	85.91	99.70	99.98
IBAUNet [58]	0.075	0.045	4.830	2.841	86.79	99.73	99.99
NABNet (Proposed)	**0.075**	0.043	**4.778**	**2.511**	**87.58**	**99.82**	**99.99**

(AAMI), BP measuring systems should have a Mean Error (ME) and Standard Deviation (SD) of magnitude less than or equal to 5 mmHg and 8 mmHg, respectively. Moreover, the number of subjects to be evaluated should be more than or equal to 85. In this study, the dataset contains records from much more than 85 subjects [64].

As presented in Table 4, predictions from the NABNet best model meet both AAMI criteria. Histograms showing the distributions of Mean Errors (ME) and Mean Absolute Errors (MAE) for SBP, DBP, and MAP predictions are plotted in Fig. 4 and **Supplementary Figure S3**, respectively. Details about the AAMI standard are provided in **Appendix D**, **Supplementary Table S3**.

Statistical Analysis: The regression and Bland-Altman plots for MAP predictions from the NABNet best model are shown in Fig. 5. There is a high correlation between the target values and the ground truths, as noticeable from the regression plot in Fig. 5**(a)**. The Pearson Correlation Coefficient for MAP predictions is 0.974, indicating a strong positive correlation between the predicted values and the ground truths. For the Bland-Altman plots, the 95% significance level, which is shown by the dashed lines, spans the segment from $\mu - 1.96\sigma$ to $\mu + 1.96\sigma$, where μ and σ are the population mean and standard deviation of the distribution, respectively. For MAP, the mean and standard deviations are 6.497 and 5.141, respectively. So, MAP spanned within the range [1.356:11.638]. From Fig. 5**(b)**, it can be deduced that the presence of outliers is not severe for MAP. Another important observation from the Bland-Altman plot is that the error magnitudes remain almost similar over the whole range. So, error performances of ABP signals with extreme BP values (severe hypertension) were not affected by their high magnitude. Regression and Bland-Altman plots for SBP and DBP and relevant performance metrics are provided in **Appendix E**, **Supplementary Figures S4 to S5**. Theoretical background about the statistical parameters reported in this section has been briefed in **Appendix E**.

3.4. Ablation studies

Apart from the main experiment, we performed some ablation studies to understand the effect on the ABP segmentation performance while various parameters of the segmentation network are varied. UNet being one of the simplest segmentation models has been selected for this set of experiments.

Table 4
Evaluation of AAMI Standard for BP Prediction.

	Parameters	ME(mmHg)	SD(mmHg)	Number of Subjects
Our Results	SBP	−0.678	2.969	≫85
	DBP	−0.342	1.059	
	MAP	−0.678	2.969	
AAMI Standard		$\leq \lvert 5 \rvert$ mmHg	$\leq \lvert 8 \rvert$ mmHg	≥ 85

Model Depth: The number of levels i.e., the depth of the U-Net segmentation architecture varied from shallow to deep, and the segmentation performance was observed and recorded in the **Supplementary Table S4** in **Appendix F**. Even though all predictor signals are range normalized before training, the segmented outputs were also expected to be between the same range (0 and 1), but this was not the case. It was noticed that for shallower segmentation models, the estimated signals do not only have more distortions (Fig. 6) but also fail to keep the predictions between 0 and 1. Shallower U-Net segmentation models produced rougher signals with lots of sharp edges, sometimes even extra peaks while deeper models produced smoother and better waveforms.

On the other hand, the deeper model efficiently handled any distortion in the predictor signals (PPG or ECG) in most cases. For example, as shown in Fig. 6, PPG in sample number 34,583 from test fold 1 had distortions in a few locations which did not affect the estimated ABP signal from the deeper model. Moreover, with a deeper model not only did the signal quality improve but also the signal amplitude range got closer to the desired level (0 to 1). As the model becomes deeper, ABP estimation performance gets better even without re-normalization.

Model Width: The width of the network i.e., the number of filters present in each layer of the U-Net model was gradually increased by doubling each time while monitoring the segmentation performance. From **Supplementary Table S5** in **Appendix F**, performance improved as the network was made wider (i.e., a greater number of filters or kernels per layer). The best performance was recorded when the network width was set at 128 for the first layer. Within the available resources, simultaneously deeper and wider networks (depth greater than 5 and width greater than 128) could not be used for this large dataset.

Number of Channels: PPG, PPG' (first-derivative or Velocity of PPG (VPG) or FDPPG), PPG'' (second-derivative or Acceleration of PPG (APG) or SDPPG), and ECG, four signals were used for ABP signal estimation. Channel number was varied from 1 to 4 using various combinations of these signals, as detailed in the **Supplementary Table S6** in **Appendix F**. The number of channels can be varied for both BP prediction and ABP estimation pipelines, making a total of 16 combinations. In practice, the number of channels for both pipelines should be maintained the same. To understand the performance patterns of BP prediction, BHS metric Grade A performance for all 16 combinations is presented in **Supplementary Table S3** as heatmaps for SBP, DBP, and MAP, respectively. The improvement in performance for SBP, DBP, and MAP with the increment of BP prediction channels reflects the gain from the BP prediction pipeline. On the contrary, when the number of input channels for ABP estimation was varied, the performance for SBP and DBP remained fixed along BP estimation channels since this experiment was performed only on re-normalized ABP signals. A significant improvement was seen in MAP estimation moving from channel 1 (only PPG) to channel 2 (PPG and ECG).

Deep Supervision: We applied Deep Supervision [69] and employed

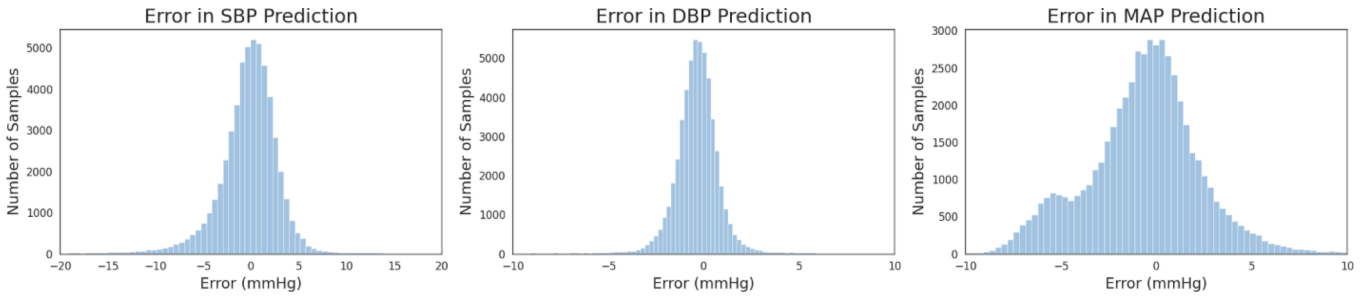

Fig. 4. Histogram showing Mean Error Distribution in SBP, DBP, and MAP predictions, respectively against the AAMI standard.

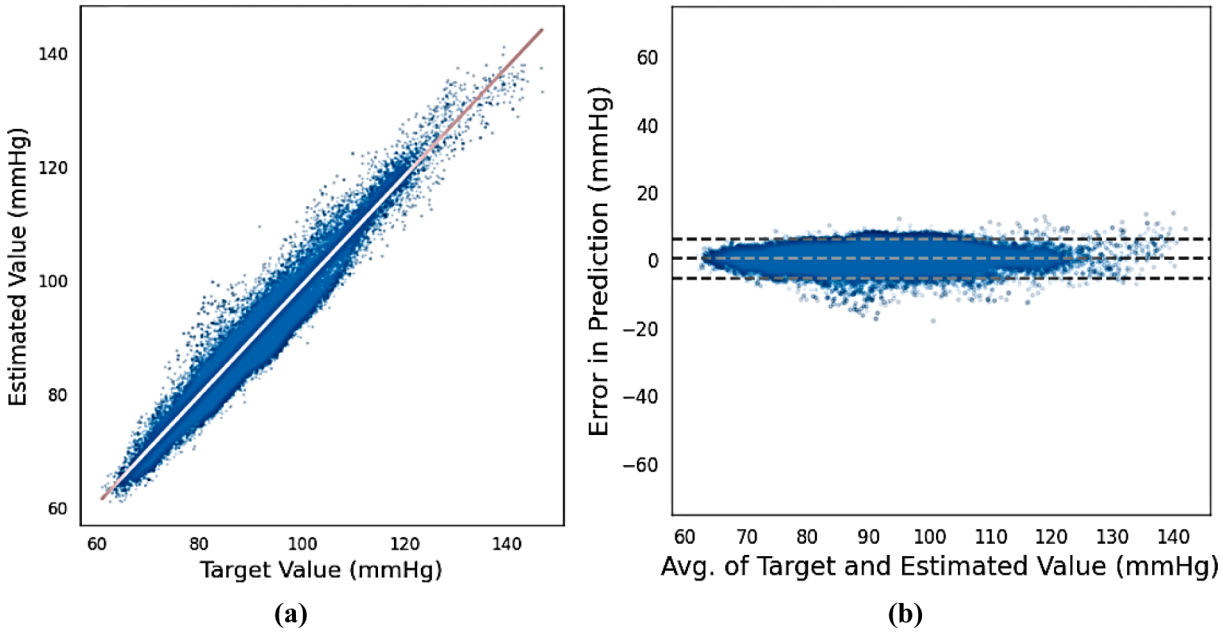

Fig. 5. **(a)** Regression and **(b)** Bland-Altman Plots for MAP Prediction.

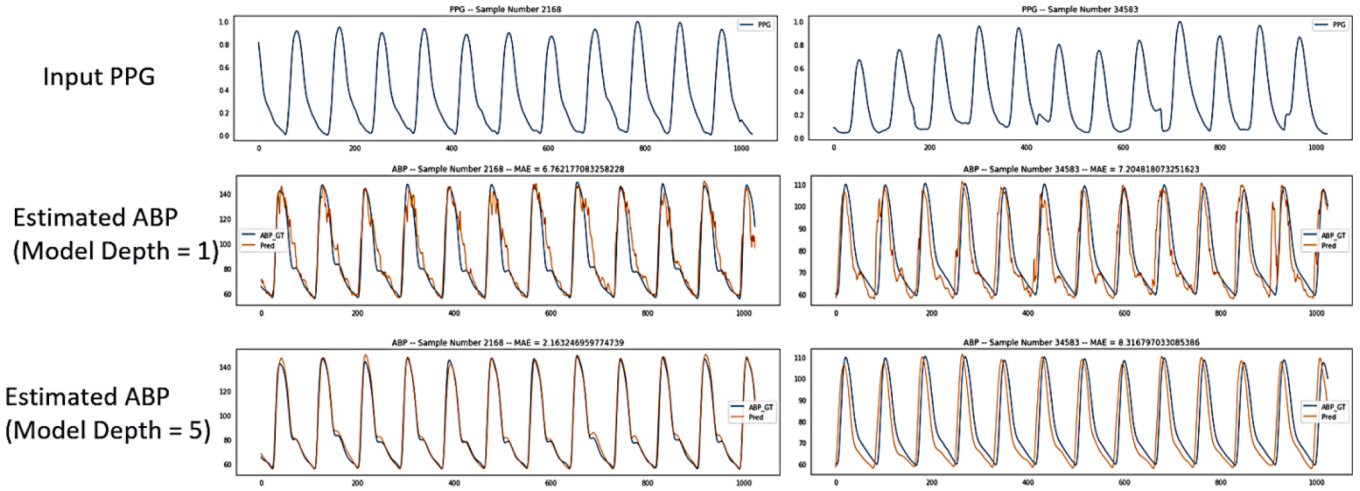

Fig. 6. Estimated ABP signal samples from Shallow and Deep U-Net models. Here, the blue color signal is the ground truth ABP signal while the orange waveform is the estimated ABP.

auxiliary losses on the Deep U-Net segmentation network for ABP waveform estimation. It has been reported in a few studies that Deep Supervision improves segmentation performance [70]. We employed additional loss operations on each deeply supervised output of the encoder. The weights of the outputs were decreased for premature outputs from the deeper layers. For example, the loss weight array for a five-layer U-Net was set as [1.0, 0.9, 0.8, 0.7, 0.6, 0.5] i.e., the final output was provided with the highest weight of 1.0 and gradually diminished. As reported in **Supplementary Table S7** in **Appendix F**, using Deep Supervision for waveform estimation improved performance

significantly, especially for SBP.

Phase-shift Correction during Data Preprocessing: There have been some studies that reported better results by correcting existing phase shifts among PPG, ECG, and ABP signals during data preprocessing [37,41]. So, for this experiment, we corrected the phase shifts among PPG, ECG, and ABP signals in the training set following the Algorithm provided in **Appendix B**. Signals before and after phase-shift correction are shown in **Supplementary Figure S2**. As reported in **Supplementary Table S8** in **Appendix F**, correcting phase-shift deteriorated the performance since it was not corrected in the test set. So, the NABNet with BiConvLSTM blocks was designed to mitigate the effect of phase-shift.

Based on these experiments, the best pipeline configurations for NABNet and other segmentation models were determined during the final experiment and the performances are tabulated in Table 3.

3.5. Qualitative evaluation

In this section, we will try to qualitatively evaluate the robustness of our approach for ABP waveform estimation in various aspects. As discussed in the introductory section, very few studies so far tried to estimate the continuous ABP waveform instead of predicting discrete BP readings. Among the studies published in this domain, to the best of our knowledge, none tried to properly evaluate the quality of their reconstructed waveforms while considering the reflectance of the change in PPG morphology, heart rate variability, cardiovascular diseases (CVDs) in the estimated ABP signals, which we will try to do in this section.

Variability in PPG morphology, Pulse Arrival Time, and Heart

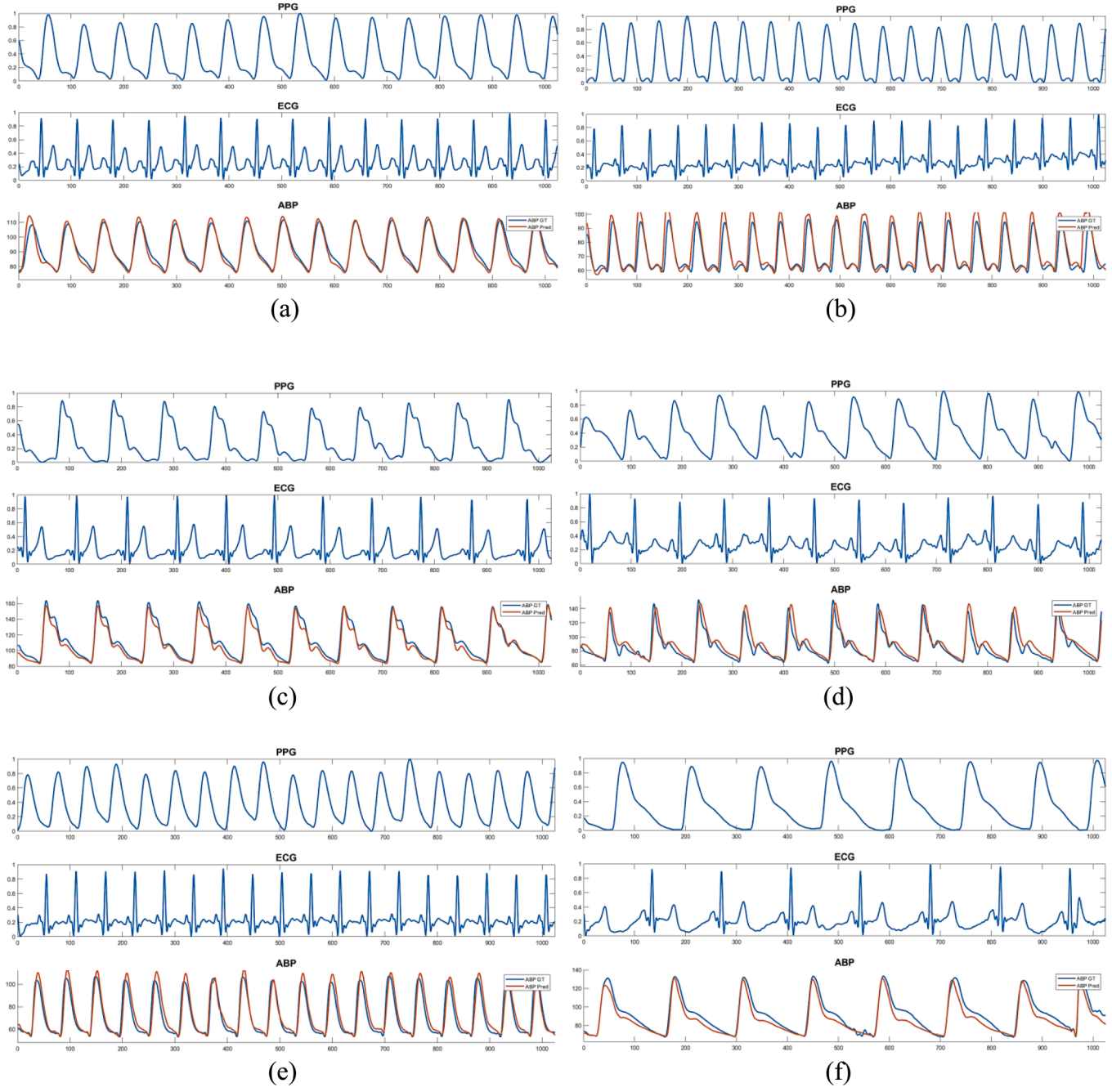

Fig. 7. Estimated ABP waveforms from PPG and ECG signals from a wide range of morphology and a varying amount of phase shifts and frequency, proving the robustness of the model.

Rate: The morphology of PPG can change due to many factors such as contact pressure during PPG acquisition (e.g., cuff pressure) [71], blood pressure level [72], ageing [73], location of data acquisition (finger, wrist, feet, forehead, etc.) [74–75], the filter used for data pre-processing [76], etc. Since the change in the morphology of ABP is simultaneous to the change in PPG, a robust model should be able to map the change in PPG into ABP given that it has been trained with enough variability and quantity of data, and the MIMIC dataset contains both of these properties. On the other hand, Pulse Arrival Time or PAT between PPG, ECG, and ABP signals can vary due to factors such as hypertension [75–77], which causes phase shifts, and it varies among subjects and time. The model should also be able to handle signals of various frequencies since heart rate varies a lot among subjects due to various reasons. As shown in Fig. 7, our model could estimate ABP waveforms from various types of PPG and ECG signals with a varying amount of phase shift and frequency. Here, the blue waveforms represent the ground truth signals.

Here, PPG and ABP patterns for normotension, pre-hypertension, and hypertension cases closely match with the plots shown in [72]. Mentionable that the PPG signals recorded in the MIMIC-III dataset should not be affected by contact pressure or data acquisition location since they are clinically collected finger PPG signals [46].

Cardiovascular Anomalies: MIMIC-III is a dataset collected mostly from patients in the Intensive Care Unit (ICU) [46], so there are many cases where traces of cardiovascular diseases (CVDs) can be noticed in the signals. The signals being recorded simultaneously, the presence of anomalies such as Atrial Fibrillation (AF) are often present in the signals. As annotated in Fig. 8, our proposed model managed to identify the anomalies from the input PPG and ECG signals and reflected them into the estimated ABP signals which matched greatly with the ground truth ABP.

Here in Fig. 8**(a) and 8(b)**, the abnormal beats in PPG and ECG have been closely estimated by the model in the estimated ABP waveform as the blood pressure dropped during those instances. In the case of Fig. 8 (c), multiple anomalies can be noticed along the waveforms. ECG in Fig. 8**(d)** has a missing R-peak, which resulted in steep slopes in the corresponding PPG and ABP beats. The model managed to estimate this correctly. Some additional figures are provided in **Appendix G**, **Supplementary Figures S6 to S10**. Mentionable that extremely anomalous signals have been removed during data preprocessing since those are beyond the scope of this study.

3.6. Comparison to the current literature

As discussed earlier, most of the studies in this domain reflected upon predicting only discrete BP values (SBP and DBP). Some of them also tried to predict discrete MAP or MBP (Mean Blood Pressure) values either through labeling from ABP waveforms, or from SBP and DBP using **Equation (12)**, but not the ABP waveform itself, e.g., [27].

$$\mathrm{MAP} = \frac{\mathrm{SBP} + (2{*}\mathrm{DBP})}{3} \tag{12}$$

Since this study aims at estimating the ABP waveform itself, the comparison was mainly performed with similar studies. Table 5 mentions some studies which utilized 1D-CNN-based deep learning techniques such as segmentation networks (e.g., UNet) [31–32,37], Variational Autoencoders (VAEs) [36], CycleGANs [45], etc. to estimate ABP waveform patterns from PPG and/or ECG signals. The comparison here is done based on Mean Absolute Error (MAE) performances for SBP, DBP, and MAP predictions from the estimated ABP signals due to this being a standard metric in this domain. Some of the studies did not report the performance in MAP prediction. Here, it can be seen that our study performed better than most of the past studies (best in terms of DBP) while having the longest duration of 435.1 h. Moreover, we

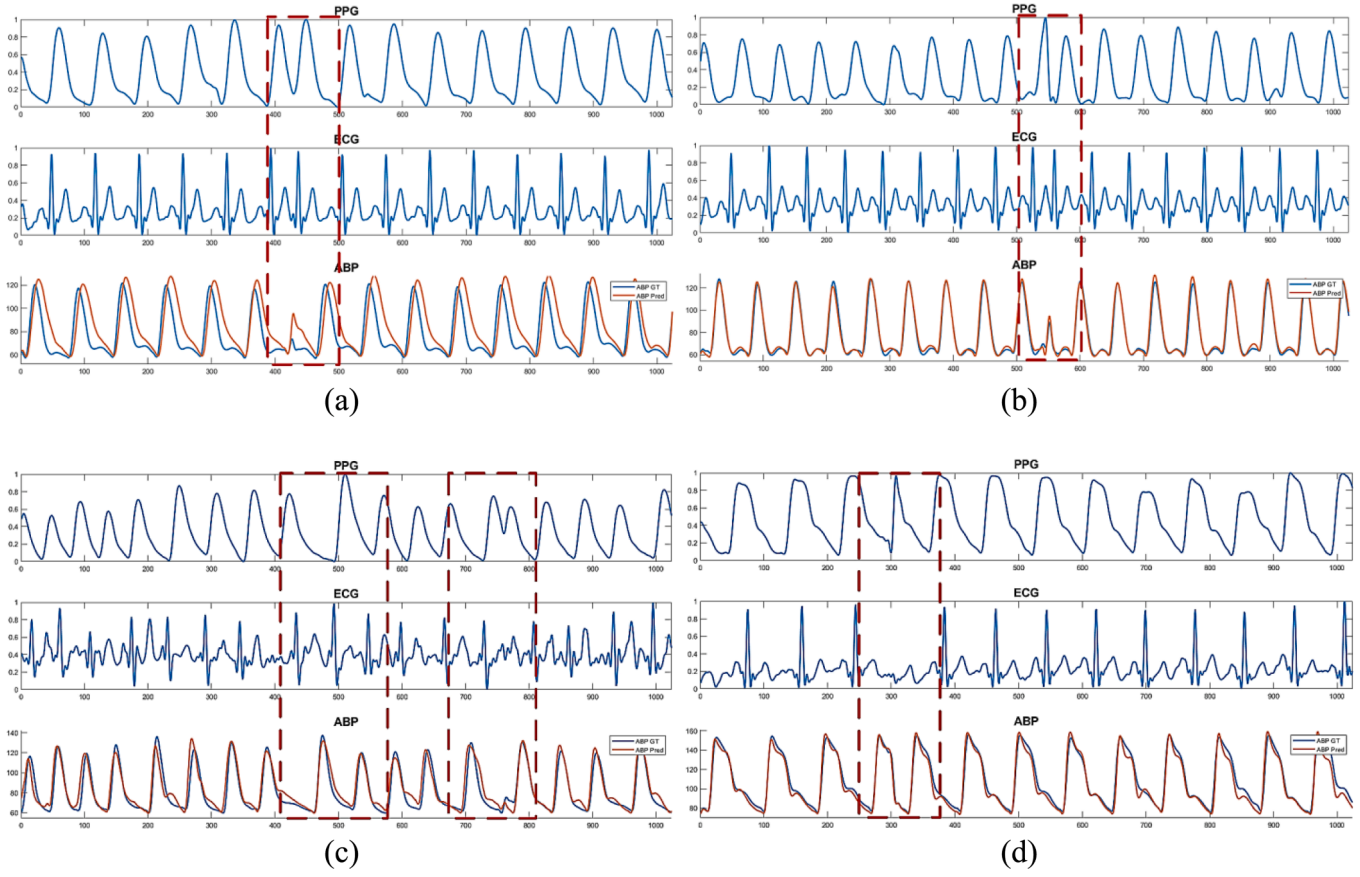

Fig. 8. Estimated ABP waveforms from PPG (and ECG) signals with annotated Cardiovascular Anomalies.

Table 5
Comparison of the proposed approach against past studies in terms of errors in BP predictions from the estimated ABP waveforms.

Study	Dataset	Records Used	Record Length (Hours)	Segments	Input Signals	MAE		
						SBP	DBP	MAP
NABNet (Proposed)	MIMIC-III (UCI)	12,000	**435.1**	191,198	PPG, ECG	2.63	**1.09**	2.37
Ibtehaz [32]	MIMIC-III (UCI)	–	353.5	127,260	PPG	5.73	3.45	2.31
Athaya [31]	MIMIC-III	100[a]	195.0	342,773	PPG	3.68	2.17	**1.97**
Harfiya [37]	MIMIC-III (UCI)	5289	≈ 48	250,000	PPG	4.05	2.41	–
Qin [36]	MIMIC-III (UCI)	1227	54.5	39,264	PPG	7.95	4.11	3.83[b]
Mehrabadi [45]	MIMIC-III	92[a]	7.7	≈ 13,800	PPG	**2.29**	1.93	–

[a] Subjects instead of Records.
[b] MAP (or MBP) has been calculated using **Equation (12)**, not the mean of the ABP waveforms.

utilized all 12,000 records from the UCI dataset which boosted the variability of our dataset. Contrary to the studies in the current literature, we also used both PPG (including PPG derivatives) and ECG signals to make the model more robust.

4. Conclusion

In conclusion, instead of estimating the ABP waveforms directly from PPG and ECG signals, this study divided the task into two sub-tasks viz. BP prediction and ABP waveform pattern estimation. Range-normalized estimated ABP patterns were linearly transformed using predicted BP values to get the complete ABP waveforms. The hybrid deep learning pipeline proposed in this study was fine-tuned through multiple sets of experiments to maximize the performance. All outcomes were taken from the estimated ABP waveforms, instead of taking BP values directly from the BP prediction pipeline to show that the BP prediction performance is not lost or altered during the process. Apart from predicting BP values, correctly estimating ABP patterns from anomalous PPG and/or ECG signals can aid in a better understanding of common cardiovascular diseases. Apart from its simplicity, the novelty of this pipeline lies also in its flexibility. Other BP prediction and/or ABP shape estimation models can easily be ensembled following this process. Moreover, the usage of this pipeline can be extended to estimate other waveforms like ABP whose absolute magnitudes carry vital information. This study used Linear Transformation to transform segmented ABP patterns into final ABP waveforms since it is the most efficient and simplest transformation method. Linear transformation also helped in making the pipeline intelligible to the readers. Non-linear transformation techniques can be explored in the future to improve the construction error and MAP prediction performance.

Data and Code Availability Statement.

The data used in this experiment along with other relevant documentation and codes used to complete this work have been made available in this GitHub repository [63].

CRediT authorship contribution statement

Sakib Mahmud: Conceptualization, Methodology, Software, Writing – original draft. **Nabil Ibtehaz:** Data curation, Writing – original draft. **Amith Khandakar:** Visualization, Investigation. **M. Sohel Rahman:** Supervision. **Antonio JR. Gonzales:** Software, Validation. **Tawsifur Rahman:** Software, Validation. **Md Shafayet Hossain:** Data curation, Writing – original draft. **Md. Sakib Abrar Hossain:** Software, Validation. **Md. Ahasan Atick Faisal:** Data curation, Writing – original draft. **Farhan Fuad Abir:** Data curation, Writing – original draft. **Farayi Musharavati:** Supervision, Writing – review & editing. **Muhammad E. H. Chowdhury:** Supervision, Writing – review & editing.

Declaration of Competing Interest

The authors declare that they have no known competing financial interests or personal relationships that could have appeared to influence the work reported in this paper.

Acknowledgment

This work was supported in part by the Qatar National Research Fund under Grant NPRP12S-0227-190164 and in part by the International Research Collaboration Co-Fund (IRCC) through Qatar University under Grant IRCC-2021-001. The statements made herein are solely the responsibility of the authors. Open access publication is supported by Qatar National Library.

Appendix A. Supplementary material

Supplementary data to this article can be found online at https://doi.org/10.1016/j.bspc.2022.104247.

References:

[1] "The top 10 causes of death", Who. int, 2021. [Online]. Available: https://www.who.int/news-room/fact-sheets/detail/the-top-10-causes-of-death.
[2] "Cardiovascular diseases", Who.int, 2021. [Online]. Available: https://www.who.int/health-topics/cardiovascular-diseases#tab=tab_1.
[3] C, Wu, H, Hu, Y, Chou, N, Huang, Y, Chou, and C, Li, "High Blood Pressure and All-Cause and Cardiovascular Disease Mortalities in Community-Dwelling Older Adults", Medicine, vol. 94, no. 47, p. e2160, 2015. Available: 10.1097/md.0000000000002160.
[4] "High blood pressure (hypertension) - Symptoms and causes", Mayo Clinic, 2021. [Online]. Available: https://www.mayoclinic.org/diseases-conditions/high-blood-pressure/symptoms-causes/syc-20373410 (accessed on 02 October 2021).
[5] G. Thambiraj, U. Gandhi, V. Devanand, M. Umapathy, Noninvasive cuffless blood pressure estimation using pulse transit time, Womersley number, and photoplethysmogram intensity ratio, Physiol. Meas. 40 (2019), https://doi.org/10.1088/1361-6579/ab1f17.
[6] I. Sharifi, S. Goudarzi, M.B. Khodabakhshi, A novel dynamical approach in continuous cuffless blood pressure estimation based on ECG and PPG signals, Artif. Intell. Med. 97 (2018), https://doi.org/10.1016/j.artmed.2018.12.005.
[7] S. Marcus, G. Dos Alexandre, et al., Online heart monitoring systems on the internet of health things environments: a survey, a reference model and an outlook, Inf. Fusion 53 (2020) 222–239.
[8] J.L. De Moraes, M.X. Rocha, G. Vasconcelos, et al., Advances in photoplethysmography signal analysis for biomedical applications, Sensors 18 (6) (2018) 1894–1920.
[9] Y. Cemal, A. Pusic, B.J. Mehrara, Preventative measures for lymphedema: separating fact from fiction, J. Am. Coll. Surg. 213 (4) (2011) 543–551, https://doi.org/10.1016/j.jamcollsurg.2011.07.001.
[10] S. Romagnoli, Z. Ricci, D. Quattrone, et al., Accuracy of invasive arterial pressure monitoring in cardiovascular patients: an observational study, Crit. Care 18 (6) (2014) 644, https://doi.org/10.1186/s13054- 014- 0644- 4.
[11] O. Takayoshi, K. Masahiro, M. Hirohito, A. Kei, O. Taku, H. Junichiro, et al., Prognosis of "masked" hypertension and "white-coat" hypertension detected by 24-h ambulatory blood pressure monitoring: 10-year follow-up from the Ohasama study, J. Am. Coll. Cardiol. 46 (3) (2005) 508–515.
[12] L. Bonsall, Calculating the mean arterial pressure (MAP), the- map, 2011.
[13] E.A, Wehrwein, M.J, Joyner, Regulation of blood pressure by the arterial baroreflex and autonomic nervous system, in: R.M. Buijs, D.F.B.T.H.o. N. Swaab (Eds.), Handbook of Clinical Neurology, Vol.
[14] G. Thambiraj, U. Gandhi, V. Devanand, M. Umapathy, Noninvasive cuffless, blood pressure estimation using pulse transit time, Womersley number, and photoplethysmogram intensity ratio, Physiol. Meas. 40 (2019), https://doi.org/10.1088/1361-6579/ab1f17.
[15] G. Thambiraj, U. Gandhi, U. Mangalanathan, J.M.J. Valanarasu, M. Anand, Investigation on the effect of Womersley number, ECG and PPG features for cuffless

blood pressure estimation using machine learning, Biomed. Signal Process. Control 60 (2020), 101942, https://doi.org/10.1016/j.bspc.2020.101942.
[16] E. Monte-Moreno, Non-invasive estimate of blood glucose and blood pressure from a photoplethysmograph by means of machine learning techniques, Artif. Intell. Med. 53 (2011) 127–138, https://doi.org/10.1016/j.artmed.2011.05.001.
[17] M. Kachuee, M.M. Kiani, H. Mohammadzade, M. Shabany, Cuff-less blood pressure estimation algorithms for continuous health-care monitoring, IEEE. Trans. Biomed. Eng. 64 (2016) 1, https://doi.org/10.1109/TBME.2016.2580904.
[18] X.M. Xing, M.S. Sun, Optical blood pressure estimation with photoplethysmography and FFT-based neural networks, Biomed, Opt. Express 7 (2016) 3007–3020, https://doi.org/10.1364/BOE.7.003007.
[19] D. Fujita, A. Suzuki, K. Ryu, PPG-based systolic blood pressure estimation method using PLS and level-crossing feature, Appl. Sci. 9 (2019) 304, https://doi.org/10.3390/app9020304.
[20] S. Bose, N. Sree, K. Arumugam, Sparse representation of photoplethysmogram using K-SVD for cuffless estimation of arterial blood pressure, in: 4th International Conference on Advanced Computing and Communication Systems, 2017, pp. 1–5, https://doi.org/10.1109/ICACCS.2017.8014669, in 2017.
[21] L. Peter, N. Noury, M. Cerny, A review of methods for non-invasive and continuous blood pressure monitoring: pulse transit time method is promising? IRBM 35 (2014) https://doi.org/10.1016/j.irbm.2014.07.002.
[22] A, Esmaili, M, Kachuee, M, Shabany, Nonlinear cuffless blood pressure estimation of healthy subjects using pulse transit time and arrival time, IEEE Trans. Instrum. Meas. PP (2017) 1–10, https://doi.org/10.1109/TIM.2017.2745081.
[23] F, Miao, Z.D, Liu, J.K, Liu, B, Wen, Y, Li, Multi-sensor fusion approach for cuff-less blood pressure measurement, IEEE J. Biomed. Health PP (2019) 1, https://doi.org/10.1109/JBHI.2019.2901724.
[24] M. Forouzanfar, H. Dajani, V. Groza, M. Bolic, S. Rajan, Feature-based neural network approach for oscillometric blood pressure estimation, IEEE Trans. Instrum. Meas. 60 (2011) 2786–2796, https://doi.org/10.1109/TIM.2011.2123210.
[25] Y.C. Hsu, Y.H. Li, C.C. Chang, L.N. Harfiya, Generalized deep neural network model for cuffless blood pressure estimation with photoplethysmogram signal only, Sensors 20 (2020), https://doi.org/10.3390/s20195668.
[26] M, Kachuee, M.M, Kiani, H, Mohammadzade, M, Shabany, Cuff-less highaccuracy calibration-free blood pressure estimation using pulse transit time, in 2015 IEEE International Symposium on Circuits and Systems, ISCAS, IEEE, 2015, pp. 1006–1009, https://doi.org/10.1109/ISCAS.2015.7168806.
[27] S.S. Mousavi, M. Firouzmand, M. Charmi, M. Hemmati, M. Moghadam, Y. Ghorbani, Blood pressure estimation from appropriate and inappropriate PPG signals using a whole-based method, Biomed. Signal Process, Control 47 (2019) 196–206, https://doi.org/10.1016/j.bspc.2018.08.022.
[28] B, Zhang, J.D, Ren, Y.Q, Cheng, B, Wang, Z.Y, Wei, Health data driven on continuous blood pressure prediction based on gradient boosting decision tree algorithm, IEEE Access PP (2019) 1, https://doi.org/10.1109/ACCESS.2019.2902217.
[29] A, Morassi Sasso et al., HYPE: Predicting Blood Pressure from Photoplethysmograms in a Hypertensive Population BT - Artificial Intelligence in Medicine. Cham: Springer International Publishing, 2020.
[30] Esmaelpoor, M. H. Moradi, and A. Kadkhodamohammadi, "A multistage deep neural network model for blood pressure estimation using photoplethysmogram signals," Comput. Biol. Med., vol. 120, no. 350, p. 103719, 2020, doi: 10.1016/j.compbiomed.2020.103719.
[31] T. Athaya, S. Choi, An estimation method of continuous non-invasive arterial blood pressure waveform using photoplethysmography: a u-net architecture-based approach, Sensors 21 (5) (2021) 1–18, https://doi.org/10.3390/s21051867.
[32] Ibtehaz, N.; Rahman, M.S. PPG2ABP: Translating Photoplethysmogram (PPG) Signals to Arterial Blood Pressure (ABP)Waveforms using Fully Convolutional Neural Networks. arXiv 2020, arXiv:2005.01669.
[33] Y.H. Li, L.N. Harfiya, K. Purwandari, Y. Der Lin, Real-time cuffless continuous blood pressure estimation using deep learning model, Sensors (Switzerland) 20 (19) (2020) 1–19, https://doi.org/10.3390/s20195606.
[34] F, Miao et al., "Continuous blood pressure measurement from one-channel electrocardiogram signal using deep-learning techniques", Artificial Intelligence in Medicine, vol. 108, p. 101919, 2020. Available: 10.1016/j.artmed.2020.101919.
[35] S, Baker, W, Xiang, and I, Atkinson, "A hybrid neural network for continuous and non-invasive estimation of blood pressure from raw electrocardiogram and photoplethysmogram waveforms", Computer Methods and Programs in Biomedicine, vol. 207, p. 106191, 2021. Available: 10.1016/j.cmpb.2021.106191.
[36] K, Qin, W, Huang and T, Zhang, "Deep generative model with domain adversarial training for predicting arterial blood pressure waveform from photoplethysmogram signal", Biomedical Signal Processing and Control, vol. 70, p. 102972, 2021. Available: 10.1016/j.bspc.2021.102972.
[37] L. N, Harfiya, C. C, Chang, and Y. H, Li, "Continuous blood pressure estimation using exclusively photoplethysmography by lstm-based signal-to-signal translation," Sensors, vol. 21, no. 9, 2021, doi: 10.3390/s21092952.
[38] L, Pradenas, "A Novel Non-Invasive Estimation of Arterial Blood Pressure from Electrocardiography and Photoplethysmography Signals using Machine Learning", Biomedical Journal of Scientific & Technical Research, vol. 30, no. 1, 2020. Available: 10.26717/bjstr.2020.30.004883.
[39] B, Hill et al., "Imputation of the continuous arterial line blood pressure waveform from non-invasive measurements using deep learning", Scientific Reports, vol. 11, no. 1, 2021. Available: 10.1038/s41598-021-94913-y.
[40] P, Li, T, Laleg-Kirati, "Central Blood Pressure Estimation From Distal PPG Measurement Using Semiclassical Signal Analysis Features", IEEE Access, vol. 9, pp. 44963-44973, 2021. Available: 10.1109/access.2021.3065576.
[41] M, Salah, O, Omer, L, Hassan, M, Ragab, A, Hassan, and A, Abdelreheem, "Beat-Based PPG-ABP Cleaning Technique for Blood Pressure Estimation", IEEE Access, vol. 10, pp. 55616-55626, 2022. Available: 10.1109/access.2022.3175436.
[42] M, Rong and K, Li, "A multi-type features fusion neural network for blood pressure prediction based on photoplethysmography", Biomedical Signal Processing and Control, vol. 68, p. 102772, 2021. Available: 10.1016/j.bspc.2021.102772.
[43] J. Esmaelpoor, M.H. Moradi, A. Kadkhodamohammadi, A multistage deep neural network model for blood pressure estimation using photoplethysmogram signals, Comput. Biol. Med. 120 (350) (2020), 103719, https://doi.org/10.1016/j.compbiomed.2020.103719.
[44] S. Mahmud, et al., A Shallow U-Net Architecture for Reliably Predicting Blood Pressure (BP) from Photoplethysmogram (PPG) and Electrocardiogram (ECG) Signals, Available, Sensors 22 (3) (2022) 919, https://www.mdpi.com/1424-8220/22/3/919.
[45] M, Mehrabadi, S, Aqajari, A, Zargari, N, Dutt, and A, Rahmani, "Novel Blood Pressure Waveform Reconstruction from Photoplethysmography using Cycle Generative Adversarial Networks", arXiv.org, 2022. [Online]. Available: https://doi.org/10.48550/arXiv.2201.09976. [Accessed: 21- Aug- 2022].
[46] Physionet.org. 2021. MIMIC-III Waveform Database v1.0. [online] Available at: <https://physionet.org/content/mimic3wdb/1.0/>.
[47] T. Pereira et al., "Photoplethysmography based atrial fibrillation detection: a review", npj Digital Medicine, vol. 3, no. 1, 2020. Available: 10.1038/s41746-019-0207-9.
[48] J, Wang, "Automated detection of atrial fibrillation and atrial flutter in ECG signals based on convolutional and improved Elman neural network", *Knowledge-Based Systems*, vol. 193, p. 105446, 2020. Available: 10.1016/j.knosys.2019.105446.
[49] H. P, W, RWCGR, M. J, W. C, S. F, A series of case studies on detection of spontaneous pulse by photoplethysmography in cardiopulmonary resuscitation, AM. J. Emerg. Med. 38 (2019) https://doi.org/10.1016/j.ajem.2019.05.044. J.
[50] G. Martínez, N. Howard, D. Abbott, K. Lim, R. Ward, M. Elgendi, Can photoplethysmography replace arterial blood pressure in the assessment of blood pressure? J. Clin. Med. 7 (2018) 316, https://doi.org/10.3390/jcm7100316.
[51] K, Bayoumy et al., "Smart wearable devices in cardiovascular care: where we are and how to move forward", Nature Reviews Cardiology, vol. 18, no. 8, pp. 581-599, 2021. Available: 10.1038/s41569-021-00522-7.
[52] "Why Data should be Normalized before Training a Neural Network", Medium, 2021. [Online]. Available: https://towardsdatascience.com/why-data-should-be-normalized-before-training-a-neural-network-c626b7f66c7d.
[53] J. Brownlee, How to use Data Scaling Improve Deep Learning Model Stability and Performance [Online]. Available: Machine Learning Mastery (2021) https://machinelearningmastery.com/how-to-improve-neural-network-stability-and-modeling-performance-with-data-scaling/.
[54] Z, Zongwei, S, Mahfuzur Rahman, T, Nima, and L, Jianming, " UNet++: Redesigning Skip Connections to Exploit Multiscale Features in Image Segmentation", arXiv.org, 2021. [Online]. Available: https://arxiv.org/pdf/1912.05074.
[55] Ozan Oktay, Jo Schlemper, Loic Le Folgoc, Matthew Lee, Mattias Heinrich, Kazunari Misawa, Kensaku Mori, Steven McDonagh, Nils Y Hammerla, et al., " Attention U-Net: Learning Where to Look for the Pancreas", arXiv.org, 2021. [Online]. Available: https://arxiv.org/abs/1804.03999.
[56] R, Azad, M, Asadi-Aghbolaghi, M, Fathy and S, Escalera, "Bi-Directional ConvLSTM U-Net with Densley Connected Convolutions", 2019 IEEE/CVF International Conference on Computer Vision Workshop (ICCVW), 2019. Available: https://ieeexplore.ieee.org/document/9022282.
[57] A, Maryam, A, Reza, F, Mahmood, and E, Sergio, " Multi-level Context Gating of Embedded Collective Knowledge for Medical Image Segmentation", arXiv.org, 2021. [Online]. Available: https://arxiv.org/abs/2003.05056.
[58] S, Chen, Y, Zou, and P, Liu, "IBA-U-Net: Attentive BConvLSTM U-Net with Redesigned Inception for medical image segmentation", Computers in Biology and Medicine, vol. 135, p. 104551, 2021. Available: https://www.sciencedirect.com/science/article/abs/pii/S0010482521003450. [Accessed 3 January 2022].
[59] M, Xiang, "Convolutions: Transposed and Deconvolution", Medium, 2022. [Online]. Available: https://medium.com/@marsxiang/convolutions-transposed-and-deconvolution-6430c358a5b6.
[60] Z. Zhang, C. Wu, S. Coleman, D. Kerr, DENSE-INception U-net for medical image segmentation, Available, Comput. Methods Programs Biomed. 192 (2020), 105395, https://www.sciencedirect.com/science/article/abs/pii/S0169260719307904.
[61] C, Li et al., "Attention Unet++: A Nested Attention-Aware U-Net for Liver CT Image Segmentation", 2020 IEEE International Conference on Image Processing (ICIP), 2020. Available: https://ieeexplore.ieee.org/document/9190761.
[62] J, Wu et al., "U-Net combined with multi-scale attention mechanism for liver segmentation in CT images", BMC Medical Informatics and Decision Making, vol. 21, no. 1, 2021. Available: https://bmcmedinformdecismak.biomedcentral.com/articles/10.1186/s12911-021-01649-w#citeas. (accessed on 16 January 2022).
[63] S, Mahmud, "NABNet", GitHub, 2021. [Online]. Available: https://github.com/Sakib1263/NABNet (accessed on 09 August 2022).
[64] "UCI Machine Learning Repository: Cuff-Less Blood Pressure Estimation Data Set", Archive.ics.uci.edu, 2022. [Online]. Available: https://archive.ics.uci.edu/ml/datasets/Cuff-Less+Blood+Pressure+Estimation.
[65] D. Dheeru, G. Casey, UCI Machine Learning Repository, Available at, [online] Archive.ics.uci.edu. (2017).
[66] "Cuff-Less Blood Pressure Estimation", Kaggle.com, 2022. [Online]. Available: https://www.kaggle.com/datasets/mkachuee/BloodPressureDataset (accessed on 21 August 2022).

[67] R. Olaf, F. Philipp and B. Thomas, " U-Net: Convolutional Networks for Biomedical Image Segmentation", arXiv.org, 2021. [Online]. Available: https://arxiv.org/abs/1505.04597.
[68] N. Ibtehaz, M. Rahman, MultiResUNet: Rethinking the U-Net architecture for multimodal biomedical image segmentation, Available, Neural Networks 121 (2020) 74–87, https://www.sciencedirect.com/science/article/abs/pii/S0893608019302503.
[69] L, Wang, C, Lee, Z, Tu and S, Lazebnik, "Training Deeper Convolutional Networks with Deep Supervision", arXiv.org, 2021. [Online]. Available: https://arxiv.org/abs/1505.02496.
[70] A, Turečková, T, Tureček, Z, Komínková Oplatková and A, Rodríguez-Sánchez, "Improving CT Image Tumor Segmentation Through Deep Supervision and Attentional Gates", Frontiers in Robotics and AI, vol. 7, 2020. Available: 10.3389/frobt.2020.00106.
[71] L, Suganthi and M, Manivannan, "Effect of upper arm cuff pressure on pulse morphology using photoplethysmography", 2022.
[72] G, Martínez, N, Howard, D, Abbott, K, Lim, R, Ward, and M, Elgendi, "Can Photoplethysmography Replace Arterial Blood Pressure in the Assessment of Blood Pressure?", 2022.
[73] Q. Yousef, M. Reaz, M. Ali, "The analysis of PPG morphology, Investigating the Effects of Aging on Arterial Compliance" (2022).
[74] V, Hartmann, H, Liu, F, Chen, Q, Qiu, S, Hughes, and D, Zheng, "Quantitative Comparison of Photoplethysmographic Waveform Characteristics: Effect of Measurement Site", Frontiers in Physiology, vol. 10, 2019. Available: 10.3389/fphys.2019.00198.
[75] G, Chan et al., "Multi-Site Photoplethysmography Technology for Blood Pressure Assessment: Challenges and Recommendations", Journal of Clinical Medicine, vol. 8, no. 11, p. 1827, 2019. Available: 10.3390/jcm8111827.
[76] M, Elgendi et al., "The use of photoplethysmography for assessing hypertension", npj Digital Medicine, vol. 2, no. 1, 2019. Available: 10.1038/s41746-019-0136-7.
[77] K, Welykholowa et al., "Multimodal Photoplethysmography-Based Approaches for Improved Detection of Hypertension", Journal of Clinical Medicine, vol. 9, no. 4, p. 1203, 2020. Available: 10.3390/jcm9041203.